LETTER

https://doi.org/10.1038/s41586-018-0541-0

Multi-step self-guided pathways for shape-changing metamaterials

Corentin Coulais[1,2,3]*, Alberico Sabbadini[2], Fré Vink[2] & Martin van Hecke[1,2]

Multi-step pathways—which consist of a sequence of reconfigurations of a structure—are central to the functionality of various natural and artificial systems. Such pathways execute autonomously in self-guided processes such as protein folding[1] and self-assembly[2–5], but have previously required external control to execute in macroscale mechanical systems, provided by, for example, actuators in robotics[6–9] or manual folding in origami[8,10–12]. Here we demonstrate shape-changing, macroscale mechanical metamaterials that undergo self-guided, multi-step reconfiguration in response to global uniform compression. We avoid the need for external control by using metamaterials that are made purely of passive components. The design of the metamaterials combines nonlinear mechanical elements with a multimodal architecture that enables a sequence of topological reconfigurations caused by the formation of internal self-contacts between the elements of the metamaterial. We realize the metamaterials by using computer-controlled water-jet cutting of flexible materials, and show that the multi-step pathway and final configuration can be controlled by rational design of the nonlinear mechanical elements. We also demonstrate that the self-contacts suppress errors in the pathway. Finally, we create hierarchical architectures to extend the number of distinct reconfiguration steps. Our work establishes general principles for designing mechanical pathways, opening up new avenues for self-folding media[11,12], pluripotent materials[9,13] and pliable devices[14] in areas such as stretchable electronics and soft robotics[15].

Mechanical metamaterials are structured forms of matter that can be designed to exhibit a wide range of anomalous properties[16], including negative responses[17], topological polarization[18], non-reciprocity[19] and shape morphing[9,20]. These deviations from ordinary elasticity arise from soft deformation modes, which are encoded in the internal architectures of mechanical metamaterials[16,18]. Most metamaterials feature a single soft mode, which limits their deformations to single-step pathways[20–23]. Multi-step deformations, and other advanced functionalities, require designs that have a high-dimensional deformation space spanned by multiple soft modes[9,13,24–27]. However, when actuated, competition between these soft modes leads to frustration[11,12] and spatial decay of functionality[23]. Hence, multi-modal mechanical metamaterials have so far either been actuated without explicit control

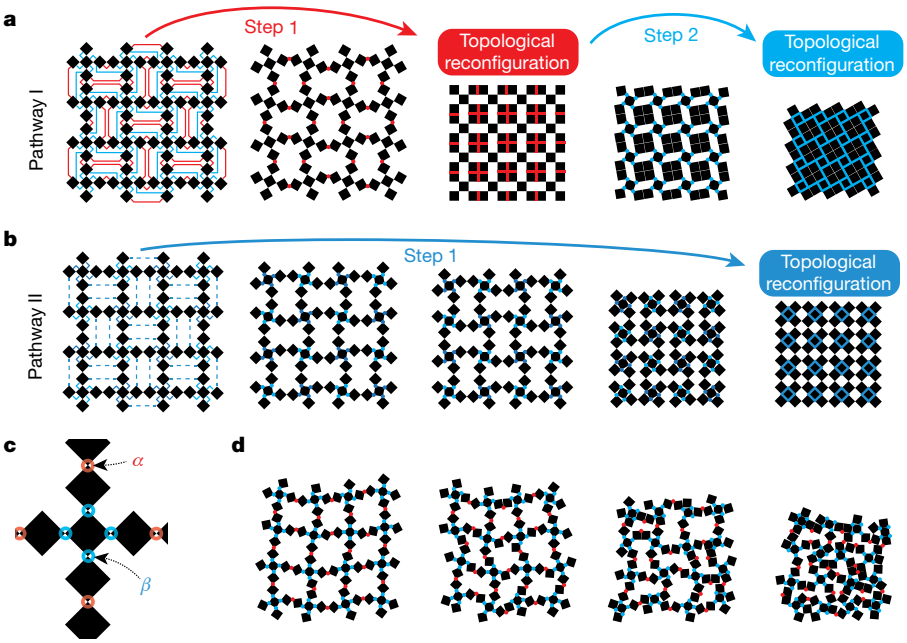

Fig. 1 | Self-guided pathways in shape-changing metamaterials. a, Two-step pathway I. In the left-most panel, the red and blue lines represent the network of self-contacts that are formed during compression. In the first step, the α links (indicated by red dots) fold and the squares connected by red lines form self-contacts (indicated in red), leading to the first topological reconfiguration; in the second step, the β links (blue dots) fold and the squares connected by blue lines form additional self-contacts (indicated in blue), leading to the second topological reconfiguration. **b**, Pathway II is a single-step pathway, in which the α links remain straight and a topological reconfiguration (blue lines) occurs after the β links are maximally folded. **c**, Close-up of the unit cell; red and blue circles indicate the α and β links and the angles α and β are defined as the deviation from the un-deformed state. **d**, Example of a disordered pathway.

[1]AMOLF, Amsterdam, The Netherlands. [2]Huygens-Kamerlingh Onnes Lab, Universiteit Leiden, Leiden, The Netherlands. [3]Institute of Physics, Universiteit van Amsterdam, Amsterdam, The Netherlands. *e-mail: coulais@uva.nl

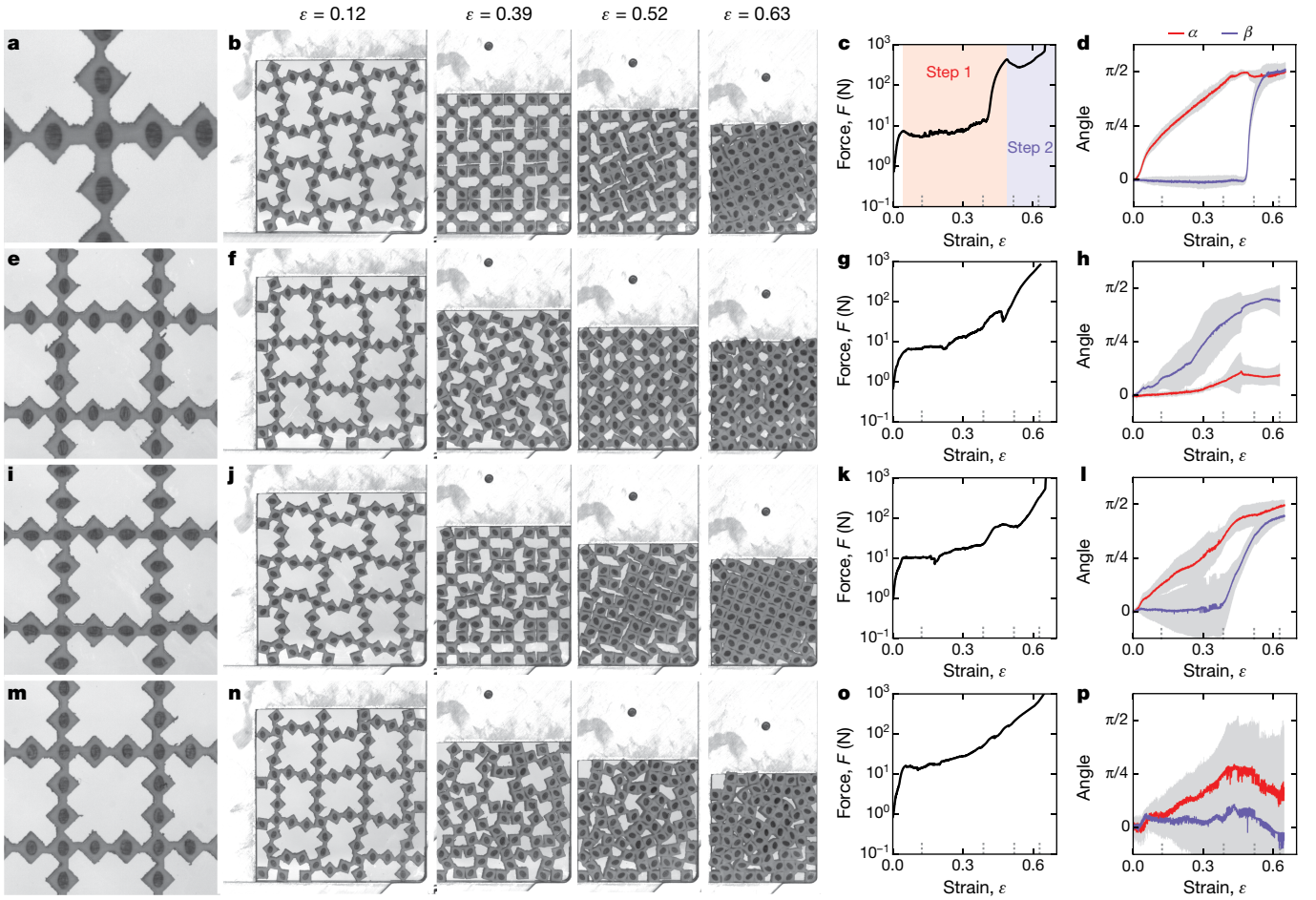

Fig. 2 | Pathway control by rational hinge design. a–d, Two-step pathway I; **e–h**, one-step pathway II; **i–l**, smoothed pathway I; **m–p**, disordered pathway. **a**, **e**, **i**, **m**, Close-ups showing hinge designs. **b**, **f**, **j**, **n**, Series of snapshots of the experimentally observed mechanical pathway, at engineering strains $\varepsilon = 0.12$, 0.39 0.52 and 0.63 (indicated by the dashed tick marks in **c**, **d**, **g**, **h**, **k**, **l**, **o** and **p**). **c**, **g**, **k**, **o**, Compressive force F versus engineering strain ε. In **c**, we indicate the two steps of the pathway. **d**, **h**, **l**, **p**, Bending of the links (α or β) versus strain ε in the central region of the sample (see Methods). See also Supplementary Video 1. The solid curves indicate the mean value of α (red) or β (blue); the grey shading indicates one standard deviation.

over their reconfiguration pathways[13,25] or required the use of multiple actuators, one for each degree of freedom[9,27]. By contrast, processes such as self-assembly[5] and protein folding[1] exhibit robust multi-step pathways without the need for external control. Here we demonstrate the design and creation of mechanical metamaterials that translate global forcing into a self-guided multi-step pathway of reconfigurations.

We consider two-dimensional metamaterials consisting of diluted lattices of freely hinged squares. We design a unit cell that consists of a cross-shaped pattern of five squares, leading to a multi-modal metamaterial of $n \times n \times 5$ squares, which allows for the formation of self-contacts between initially separated elements and has $3n^2 + 4n - 3$ zero-energy modes (Fig. 1, Methods). This structural design admits a two-step deformation pathway (which we refer to as pathway I; see Fig. 1), characterized by the deformation angles α and β (Fig. 1a, c). In the first step of pathway I, the α links fold whereas the β links remain fixed until self-contacts, which change the topology of the material, are formed. This topological reconfiguration spawns a daughter structure. In the second step, the α links remain fixed and the β links fold until the system is fully compacted (Fig. 1a). This is one possible deformation pathway, but our structure admits many other pathways, some of which are highly structured (such as pathway II; see Fig. 1b, Methods) and most of which are disordered (Fig. 1d).

To obtain a specific deformation path in response to global compression, we augment this structural design with suitably tailored mechanical interactions by connecting the squares with beam-like links of varying thickness t_α and t_β (Methods). This replaces the zero-energy modes with soft modes, the energetics of which are controlled by the links. These beams also introduce a well-defined critical compressive load proportional to t^3, above which the nonlinear buckling instability causes spontaneous bending of the corresponding link[28]. Intuitively, pathway I requires that $t_\alpha < t_\beta$, whereas pathway II requires $t_\beta < t_\alpha$ (Fig. 1). The mode structures in the corresponding asymptotic limits reveal an important qualitative difference: whereas the un-deformed metamaterial has a single soft mode for $t_\alpha \ll t_\beta$, it has many $(n^2 + 6n - 3)$ soft modes for $t_\beta \ll t_\alpha$ because the numerous soft β links can deform in many ways in this case (Methods). This counting argument suggests that pathway I will be much easier to realize than pathway II.

To design the links rationally to obtain either pathway I or pathway II, we analysed the modes and instabilities of a representative volume element—a super-cell consisting of a 2×2 grid of unit cells—as function of t_α and t_β (Methods). This modal analysis substantiates our counting-based argument. First, we find that it is the ratio t_α/t_β, rather than the individual thicknesses, that is important. Moreover, for small t_α/t_β, the first buckling mode corresponds to the first step in pathway I, with other modes strongly suppressed. Finally, for large t_α/t_β, even though the first buckling mode coincides with the first step in pathway II, other modes remain in competition. From the details of this analysis we extract specific design guidelines for the rational design of the link parameters (Methods).

We illustrate our approach experimentally. We used a water-jet cutter to fabricate reconfigurable metamaterials with squares of size 4.5 mm

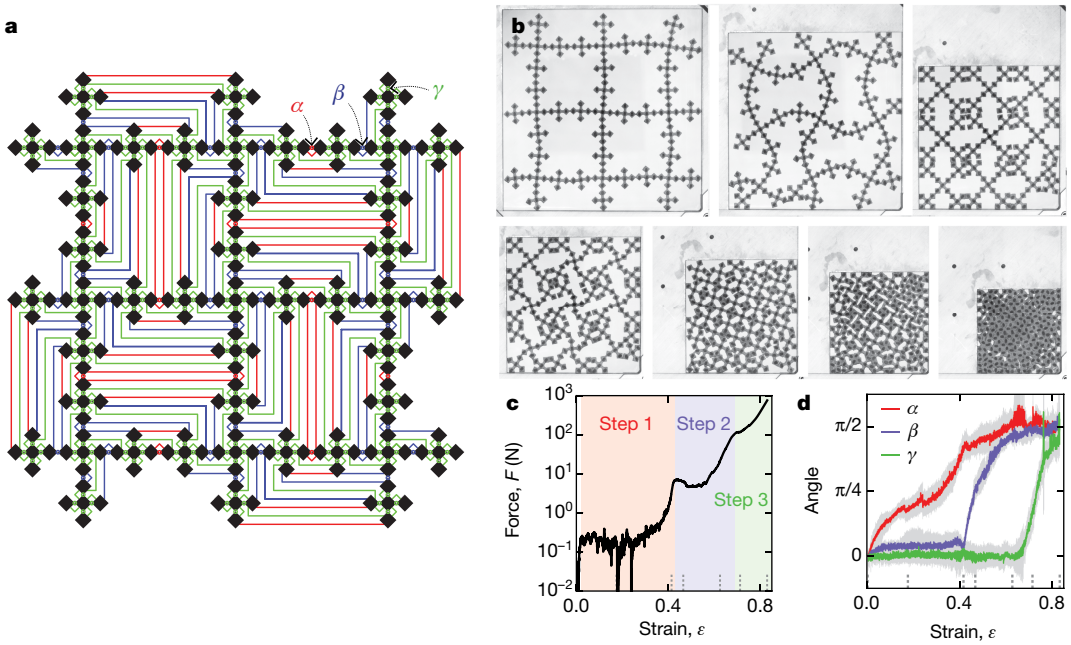

Fig. 3 | Three-step mechanical pathway. a, Geometry of a shape-changing hierarchical metamaterial. The red, blue and green coloured circles indicate the α, β and γ links, respectively. The red, blue and green coloured lines indicate the self-contacts between the squares (indicated in black) that form upon the subsequent folding of the α, β and γ links. **b**, Snapshots of the experimentally observed three-step mechanical pathway at $\varepsilon = 0$, 0.20, 0.37, 0.58, 0.62, 0.70 and 0.85 (indicated by the dashed tick marks in **c** and **d**). See also Supplementary Video 2. **c**, Compression force F versus engineering strain ε. **d**, Bending angles of the links (α, red; β, blue; γ, green) versus engineering strain ε. Lines, mean; shading, one standard deviation.

out of rubber sheets that are 10 mm thick (this prevents out-of-plane buckling). We then actuated their deformation pathways by applying a uniform equi-biaxial strain ε while tracking the compressive force, the motion of each element and the evolution of the folding angles α and β (see Methods). We focus on four different samples that share the same structural design but differ in their α and β links, which are designed to obtain one of four specific pathways (Fig. 2a, e, i, m).

We first design a metamaterial that follows the two-step pathway I. Following our design guidelines (Methods), we take $t_\alpha = 1.0$ mm and $t_\beta = 2.0$ mm (Fig. 2a). Under compression, the α links buckle at a strain of 4%, triggering the counter-rotation mode[22] and the first step of the reconfiguration pathway (Fig. 2b). Further compression does not substantially increase the force[28], preventing buckling of the stronger β links, until self-contacts are formed at a strain of 49%. The ensuing topological reconfiguration gives rise to a daughter structure with only one soft mode governed by the β links. Further compression leads to a steep rise in the compressive force, which triggers the buckling of the β links and initiates the second reconfiguration step; this second step continues until the structure is fully compressed (Fig. 2b). The compressive force clearly shows the plateaus associated with buckling and the rapid increase associated with the formation of self-contacts (Fig. 2c). This multi-step pathway is fully consistent with the theoretical pathway I, as further demonstrated by the distinct evolution of the angles α and β as functions of strain (Fig. 2d, Methods). Different geometries can be designed that have similar multi-step pathways under uniaxial compression (Methods). Hence, the combination of self-contacts, buckling and topological reconfiguration enables multi-step sequences in which buckling initiates bending, and sufficient bending—or folding—creates self-contacts and topological reconfigurations, which in turn trigger more buckling events.

Successful execution of a structured pathway requires error-correcting mechanisms that compensate for distortions caused by boundary frustration and manufacturing imperfections. Although the scatter in α and β increases considerably during each deformation step, it decreases sharply upon reaching self-contact (Fig. 2d). This reduction results from the self-alignment of the flat interfaces of contacting squares and underlies the feature of our metamaterials that the fully compressed structure is highly ordered. Hence, self-contacts are crucial for error correction, ensuring robust execution of a pathway.

Pathway II is harder to realize experimentally. Even for large $t_\alpha/t_\beta = 4$ we observe that although the deformation is qualitatively similar to pathway II it is disordered, which we attribute to competition between multiple modes (Methods). To address this issue, we demonstrate that symmetry-breaking perturbations can suppress the undesired modes and promote pathway II. We introduce another design parameter, δ_β, and laterally offset the β links by distance $\delta_\beta = t_\beta/2$ with alternating chirality (Fig. 2e, Methods). The design guideline that we extracted from our numerical analysis suggests that such symmetry-breaking offsets are sufficient to favour pathway II for any t_α/t_β greater than about 2 (Methods). We therefore created a second sample with these offsets, and $t_\alpha = 2.0$ mm $> t_\beta = 0.8$ mm. We find that under compression the slender β links bend and the thicker α links remain essentially straight, resulting in a single-step pathway to a different end state (Fig. 2e–h).

Offsets can also be used to modify and probe pathway I. By fixing $\delta_\beta = t_\beta/2$ with constant chirality (Fig. 2i, m) and gradually increasing t_α/t_β, we find experimentally that up to $t_\alpha/t_\beta \approx 1.2$ the broken symmetry causes blurring of the pathway and larger scatter in the bending angles; however, we still obtain pathway I and the fully folded state is still reached, which illustrates the robustness of pathway I against perturbations (Fig. 2i–l; $t_\alpha = 1.2$ mm, $t_\beta = 1.0$ mm). For larger t_α/t_β (more than about 1.4), we observe a disordered pathway (Fig. 2m–p; $t_\alpha = 1.4$ mm, $t_\beta = 1.0$ mm). These examples with offset links demonstrate that symmetry breaking provides an efficient strategy to steer the deformation pathway.

Finally, the hierarchical nature of our structural design can be used to create metamaterials with a three-step pathway. Our two-step design results from replacing each square in a rotating square mechanism[21] with a cross-shaped pattern of five smaller squares (Methods). To obtain a three-step sequence, we replace each square in the unit cell of the two-step design with a smaller cross-shaped subpattern (Methods). The resulting unit cell consists of 25 small squares that form a generation-two box fractal; we create a metamaterial out of nine of these unit cells, which, in the limit of perfect hinges, has 216 zero modes (Fig. 3a,

Methods). We obtain a three-step pathway by sequential folding of the α, β and γ links, which leads to an intricate web of self-contacts (Fig. 3a, Methods). We tailor the three classes of links to set up this pathway by taking $t_\alpha = 1.0\ \text{mm} < t_\beta = 1.2\ \text{mm} < t_\gamma = 2.0\ \text{mm}$. Upon biaxial compression, we observe a three-step sequence of reconfigurations that leads to a fully closed, highly ordered structure (Fig. 3b, Supplementary Video 2). The compressional force and bending angles further evidence the three distinct steps of this reconfiguration pathway (Fig. 3c, d), demonstrating that our design strategy can be used to achieve complex, multiple-step pathways that are very robust.

We have shown that hierarchical structures dressed with mechanical switches based on buckling and self-contacts undergo self-guided topological reconfigurations that are robust to imperfections. Our designs are purely geometric and can therefore be applied over a range of scales; they are also passive, alleviating the need for external control. We expect our approach to enhance the potential of, for example, reconfigurable materials[9,13,29,30], soft robotics[8], origami metamaterials[10–12] and stretchable electronics[13,14].

Online content

Any methods, additional references, Nature Research reporting summaries, source data, statements of data availability and associated accession codes are available at https://doi.org/10.1038/s41586-018-0541-0.

Received: 14 January 2018; Accepted: 13 August 2018;
Published online 26 September 2018.

1. Dobson, C. M. Protein folding and misfolding. *Nature* **426**, 884–890 (2003).
2. Winfree, E., Liu, F., Wenzler, L. A. & Seeman, N. C. Design and self-assembly of two-dimensional DNA crystals. *Nature* **394**, 539–544 (1998).
3. Wei, B., Dai, M. & Yin, P. Complex shapes self-assembled from single-stranded DNA tiles. *Nature* **485**, 623–626 (2012).
4. Chen, Q., Bae, S. C. & Granick, S. Directed self-assembly of a colloidal kagome lattice. *Nature* **469**, 381–384 (2011).
5. Zeravcic, Z. & Brenner, M. P. Self-replicating colloidal clusters. *Proc. Natl Acad. Sci. USA* **111**, 1748–1753 (2014).
6. Zykov, V., Mytilinaios, E., Adams, B. & Lipson, H. Robotics: self-reproducing machines. *Nature* **435**, 163–164 (2005).
7. Shepherd, R. F. et al. Multigait soft robot. *Proc. Natl Acad. Sci. USA* **108**, 20400–20403 (2011).
8. Felton, S., Tolley, M., Demaine, E., Rus, D. & Wood, R. Applied origami. a method for building self-folding machines. *Science* **345**, 644–646 (2014).
9. Overvelde, J. T., Weaver, J. C., Hoberman, C. & Bertoldi, K. Rational design of reconfigurable prismatic architected materials. *Nature* **541**, 347–352 (2017).
10. Waitukaitis, S., Menaut, R., Chen, B. G. & van Hecke, M. Origami multistability: from single vertices to metasheets. *Phys. Rev. Lett.* **114**, 055503 (2015).
11. Pinson, M. B. et al. Self-folding origami at any energy scale. *Nat. Commun.* **8**, 15477 (2017).
12. Stern, M., Pinson, M. & Murugan, A. The difficulty of folding self-folding origami. *Phys. Rev. X* **7**, 041070 (2017).
13. Cho, Y. et al. Engineering the shape and structure of materials by fractal cut. *Proc. Natl Acad. Sci. USA* **111**, 17390–17395 (2014).
14. Xu, S. et al. Materials science: assembly of micro/nanomaterials into complex, three-dimensional architectures by compressive buckling. *Science* **347**, 154–159 (2015).
15. Rogers, J., Huang, Y., Schmidt, O. G. & Gracias, D. H. Origami mems and nems. *MRS Bull.* **41**, 123–129 (2016).
16. Bertoldi, K., Vitelli, V., Christensen, J. & van Hecke, M. Flexible mechanical metamaterials. *Nat. Rev. Mater.* **2**, 17066 (2017).
17. Bertoldi, K., Reis, P. M., Willshaw, S. & Mullin, T. Negative Poisson's ratio behavior induced by an elastic instability. *Adv. Mater.* **22**, 361–366 (2010).
18. Huber, S. D. Topological mechanics. *Nat. Phys.* **12**, 621–623 (2016).
19. Coulais, C., Sounas, D. & Alú, A. Static nonreciprocity in mechanical metamaterials. *Nature* **542**, 461–464 (2017).
20. Coulais, C., Teomy, E., de Reus, K., Shokef, Y. & van Hecke, M. Combinatorial design of textured mechanical metamaterials. *Nature* **535**, 529–532 (2016).
21. Grima, J. N. & Evans, K. E. Auxetic behavior from rotating squares. *J. Mater. Sci. Lett.* **19**, 1563–1565 (2000).
22. Mullin, T., Deschanel, S., Bertoldi, K. & Boyce, M. C. Pattern transformation triggered by deformation. *Phys. Rev. Lett.* **99**, 084301 (2007).
23. Coulais, C., Kettenis, C. & van Hecke, M. A characteristic length scale causes anomalous size effects and boundary programmability in mechanical metamaterials. *Nat. Phys.* **14**, 40–44 (2018).
24. Gatt, R. et al. Hierarchical auxetic mechanical metamaterials. *Sci. Rep.* **5**, 8395 (2015).
25. Tang, Y. et al. Design of hierarchically cut hinges for highly stretchable and reconfigurable metamaterials with enhanced strength. *Adv. Mater.* **27**, 7181–7190 (2015).
26. Mousanezhad, D. et al. Hierarchical honeycomb auxetic metamaterials. *Sci. Rep.* **5**, 18306 (2015).
27. Overvelde, J. T. et al. A three-dimensional actuated origami-inspired transformable metamaterial with multiple degrees of freedom. *Nat. Commun.* **7**, 10929 (2016).
28. Coulais, C., Overvelde, J. T. B., Lubbers, L. A., Bertoldi, K. & van Hecke, M. Discontinuous buckling of wide beams and metabeams. *Phys. Rev. Lett.* **115**, 044301 (2015).
29. Blees, M. K. et al. Graphene kirigami. *Nature* **524**, 204–207 (2015).
30. Zhang, Y. et al. A mechanically driven form of kirigami as a route to 3D mesostructures in micro/nanomembranes. *Proc. Natl Acad. Sci. USA* **112**, 11757–11764 (2015).

Acknowledgements We thank J. Mesman and D. Ursem for technical support. We acknowledge Z. Zeravcic and A. Murugan for discussions. We acknowledge funding from the Netherlands Organization for Scientific Research through grants VICI No. NWO-680-47-609 (M.v.H.) and VENI NWO-680-47-445 (C.C).

Reviewer information *Nature* thanks L. Howell and L. Valdevit for their contribution to the peer review of this work.

Author contributions All authors conceived the project. C.C. and M.v.H. developed the theoretical models and C.C. performed the numerical simulations. C.C., A.S. and F.V. designed and carried out the experiments. C.C. and M.v.H. wrote the manuscript.

Competing interests The authors declare no competing interests.

Additional information
Extended data is available for this paper at https://doi.org/10.1038/s41586-018-0541-0.
Supplementary information is available for this paper at https://doi.org/10.1038/s41586-018-0541-0.
Reprints and permissions information is available at http://www.nature.com/reprints.
Correspondence and requests for materials should be addressed to C.C.
Publisher's note: Springer Nature remains neutral with regard to jurisdictional claims in published maps and institutional affiliations.

METHODS

Hierarchical design. The architecture of our metamaterials is based on an $n \times n$ rotating-square mechanism (Extended Data Fig. 1a). We see this as the first rank in a hierarchy, and for increasing rank replace each square building block with a subpattern of five smaller squares. This construction is known as a box fractal (Extended Data Fig. 1b–d). For an $n \times n$ pattern of units of rank m, the number of squares is $n^2 \times 5^{(m-1)}$. These squares are connected by $2n(n-1)$ α links that connect different unit cells. For $m \geq 2$ there are, in addition, four internal β links per unit; for $m \geq 3$ there are, in addition, 4×5 internal γ links. In general, going from rank $m-1$ to rank m yields $4n^2 \times 5^{(m-2)}$ additional internal links. For general $m \geq 2$, this yields

$$2n(n-1) + 4n^2 \sum_{i=0}^{m-2} 5^i = -2n + n^2[1 + 5^{(m-1)}]$$

connections.

Hinged tessellations. Hinged tessellations are freely hinging structures that can be folded into a fully area-filing structure. The rotating-square mechanism is an example of a hinged tessellation (Extended Data Fig. 2a). Considering pathways in our hierarchical metamaterials, we also encounter variations on the rotating-square mechanism with unequal squares (Extended Data Fig. 2b) and crosses (Extended Data Fig. 2c); both are hinged tessellations and can form area-filling structures with multiple self-contacts.

Zero modes. When the links between the squares are completely flexible, a simple Maxwell counting argument allows us to determine the number of zero modes. We start from three degrees of freedom per square (translation and rotation) and subtract two constraints for each connection, as well as three global degrees of freedom (global translation and rotation). This yields a simple expression for the number of internal degrees of freedom n_z:

$$n_z = n^2[5^{(m-1)} - 2] + 4n - 3 \quad (1)$$

For $m=2$, $n_z = 3n^2 + 4n - 3$, yielding 61 internal zero modes for the $n=4$, rank-2 structures that we show in Figs. 1 and 2; for $m=3$, $n_z = 23n^2 + 4n - 3$, yielding 216 internal zero modes for our $n=3$, rank-3 structure (Fig. 3).

To count the number of soft modes in the limit $t_\alpha \ll t_\beta$, we consider the case in which the β links are stiff and the α links are floppy, which results in a structure that is equivalent to a rotating-square mechanism with one degree of freedom[21]. To count the number of soft modes in the limit $t_\beta \ll t_\alpha$, for $m=2$ we consider the case in which the β links are floppy and the α links are stiff; these links then impose three instead of two constraints, so that an additional $2n(n-1)$ constraints must be subtracted from equation (1), yielding $n^2 + 6n - 3$ floppy modes.

Rational design of links. In the metamaterial, we dress α links and β links with elastic beams of thicknesses t_α and t_β. Such link thicknesses control the critical buckling strains and buckling modes, with the relative thickness t_α/t_β having a crucial role. Our aim is to design these link parameters so that for each step of the pathway the required mode dominates the deformations; for the specific pathways I and II, this requires tuning t_α and t_β to obtain the first buckling mode that initiates the deformation sequence under compression.

To gain insight in the role of the link thicknesses, we take the following general design approach. First, we calculate the spectrum of soft modes at zero strain as a function of t_α and t_β, and decompose the spatial structure of the lowest-energy mode onto a basis of 'motions', which correspond to desired (and undesired) pathway steps. Although a pathway consists of highly nonlinear deformations, this linear analysis still provides important insights into the role of the link parameters. Second, we perform a nonlinear analysis to determine the critical strain and spatial structure of the first buckling mode, as functions of the link parameters. Altogether, this analysis leads to the rational design of the links to generate a desired deformation pathway.

Motions. To focus on the essential physics, we define a system of four unit cells, organized in a 2×2 super-cell and placed in a uniformly compressed square box with periodic boundary conditions. In a general $n \times n$ system, periodic boundaries tie the nodes at the left (bottom) boundary to the nodes at the right (top) boundary, leading to $4n$ constraints. To remain compatible with the experimental boundary conditions, we require that the super-cell fits in a square box: the n edges at each side are required to be aligned, leading to an additional $2(n-1)$ constraints, and the horizontal and vertical dimensions are required to be equal, leading to a single additional constraint. Hence, in the limit of flexible hinges, the number of zero modes with square periodic boundary conditions is

$$n_z^{\text{periodic}} = n^2[5^{(m-1)} - 2] - 2n - 2$$

For an $m=2$, $n=2$ super-cell with square periodic boundary conditions, we thus find six zero modes. We define a vector $\boldsymbol{b}$ that describes the bending of the links (see Extended Data Fig. 3a, b) and construct an appropriate orthogonal basis $\boldsymbol{m}_{\text{A},\ldots,\text{F}}$ which we refer to as motions A–F (see Extended Data Fig. 3c, d). We choose motions A and B to coincide with the first step of pathways I (Fig. 1a) and II (Fig. 1b), and use the motions to characterize the soft modes and buckling modes.

Linear modes. We calculated the softest eigenmodes at zero strain as functions of t_α and t_β using a finite-element method (see Methods section 'Numerical simulations'). We fix $t_\alpha + t_\beta$ to be 1 mm, 2 mm or 3 mm and focus on the role of t_α/t_β, because we find that the sum $t_\alpha + t_\beta$ has a very minor role for the mode structures. We find that for small values of t_α/t_β one mode is much softer than all others, whereas for larger values of t_α/t_β several modes are in close competition (Extended Data Fig. 4a). Consistent with our counting argument, this finding can be understood by noting that when $t_\alpha \ll t_\beta$ only motion A is soft, whereas when $t_\beta \ll t_\alpha$ motions B–E are all soft, with the eigenmodes mixing these motions.

By characterizing the spatial structure of the softest mode by projecting it onto the motions A–F, we obtain the following scenario. First, there is a broad crossover regime in which multiple motions are important, with the crossover centred around $t_\alpha/t_\beta \approx 1.5$, consistent with the fact that there are more β links than α links. Second, for small values of t_α/t_β motion A dominates, whereas at large values of t_α/t_β motions B and C both have a role (Extended Data Fig. 4b). Together, this analysis suggests that for sufficiently small t_α/t_β, where the lowest mode is well isolated and corresponds closely to motion A, pathway I can be robustly obtained, whereas the situation for large t_α/t_β is more complex, with multiple modes and motions in competition.

Buckling modes. To fully understand the role of t_α/t_β, we performed a stepwise nonlinear analysis and calculated the critical strain at which the first mode becomes unstable, and similarly projected the corresponding nonlinear buckling mode onto the six motions A–F (Extended Data Fig. 4c, d). These data confirm a crossover at $t_\alpha/t_\beta \approx 1.5$. The buckling modes can be expressed almost completely as a combination of motions A and B, with other motions suppressed and essentially irrelevant.

Symmetry-broken links. Execution of pathway II is more difficult than pathway I, presumably because of the large number of competing modes and motions with deformations of the β links. However, it is possible to select pathway II, even for moderate values of the thickness ratio t_α/t_β, by introducing a symmetry-breaking lateral offset in the β links. We fix the offset magnitude of this additional design parameter to be $|\delta_\beta| = 0.5t_\beta$ (so the symmetry breaking is either on or off) and focus on offset patterns consistent with motion B. We then run full nonlinear simulations on a 2×2 super-cell with square periodic boundary conditions for a range of values of t_α/t_β while $t_\alpha + t_\beta = 3$ mm is fixed. To illustrate the general scenario, we show snapshots of the un-deformed and deformed system for $t_\alpha/t_\beta = 0.4$ and $t_\alpha/t_\beta = 2.3$ in Extended Data Fig. 5a, b. In both cases there is no instability and the deformation is smooth. At large strains we observe the deformed state corresponding to motion A for $t_\alpha/t_\beta = 0.4$, illustrating that motion A is favoured for small t_α/t_β even in the presence of offsets that promote motion B. However, for larger t_α/t_β the large strain deformation corresponds to motion B, illustrating that a combination of symmetry-breaking offsets and large t_α/t_β allows pathway II to be initiated (Extended Data Fig. 5c, d).

Design guidelines and experimental validation. We now turn our numerical observations of the crossovers between different behaviours as function of t_α/t_β, with and without offsets, into practical design guidelines, noting that there are no sharp boundaries. First, we expect that pathway I should be observed without offsets whenever t_α/t_β is less than about 1, with increasing fidelity for smaller ratios; for example, for $t_\alpha/t_\beta = 0.5$, the overlap between the buckling mode and motion A is more than 90% (Extended Data Fig. 4d). Second, to obtain pathway II, we suggest combining an offset and large values of t_α/t_β. For the specific offset magnitude used here ($|\delta_\beta| = 0.5t_\beta$) and an offset pattern of alternating chirality, concomitant with motion B, our data show that for t_α/t_β greater than about 2 motion B dominates; for example, for $t_\alpha/t_\beta = 2.3$, the overlap between the nonlinear mode and motion B is already 75% (Extended Data Fig. 5c, d). Finally, we note that link thicknesses much less than 1 mm are not experimentally feasible and link thicknesses larger than a few millimetres become comparable to the size of the square elements, providing practical constraints on our design space.

Experimental validation of pathway I. We performed experiments without offset, with $t_\alpha/t_\beta = 0.5$ (Fig. 2a–d) and $t_\alpha/t_\beta = 0.4$ (not shown), that show a clear pathway I; we also performed an experiment without offset and with $t_\alpha/t_\beta = 1.4$ that shows a disordered pathway (not shown). Earlier experiments with less accurately manufactured 3D-printed samples also showed clear pathway I deformations, so we conclude that pathway I is robust for t_α/t_β less than about 1. In addition, we performed experiments with an offset pattern of constant chirality, consistent with motion E, for $t_\alpha/t_\beta = 1$, 1.2, 1.4, 1.5 and 2.5; the first two values lead to smoothed versions of pathway I and the last three to disordered pathways (Fig. 2).

Experimental validation of pathway II. We attempted to obtain pathway II experimentally without offset and with $t_\alpha/t_\beta = 4$. Despite the fact that a large part of the sample follows motion B, these samples also display a large amount of disorder, seemingly nucleating near the boundaries, which prevents a successful execution of pathway II (Extended Data Fig. 6). We therefore performed experiments with an offset $|\delta_\beta| = 0.5t_\beta$ and an alternating chirality consistent with motion B (Fig. 2).

We find that pathway II can be obtained for moderate values of $t_\alpha/t_\beta = 2$ (not shown) and $t_\alpha/t_\beta = 2.5$ (Fig. 2).

Numerical simulations. For the finite-elements simulations of a representative metamaterial element we use the commercial software Abaqus/Standard.

Model definition. We model 2×2 super-cells of our metamaterials, varying the parameters t_α, t_β and the offset δ_β (Extended Data Fig. 7), using a neo-Hookean energy density as a material model, a shear modulus $G = 2.7$ MPa, bulk modulus $K = 133$ GPa (or equivalently a Young's modulus $E = 8.0$ MPa and Poisson ratio $\nu = 0.49999$) and plane stress conditions with hybrid quadratic triangular elements (Abaqus type CPS6). We construct the mesh so that the thinnest parts of the samples are at least two elements across. As a result, the unit cells of the metamaterial have approximately 10^4 triangular elements.

Boundary conditions. To implement periodic square boundary conditions, we define constraints on the displacements of all of the nodes at the horizontal and vertical boundaries of the unit cell[31]. In addition, we ensure that the periodic boundary remains square-shaped.

Analysis. We perform three types of analysis: linear eigenmodes analysis, where we calculate the lowest eigenmodes and their eigenfrequencies (Extended Data Fig. 4a, b); nonlinear bifurcation analysis, where we perform a stepwise nonlinear stability analysis to determine the bifurcation point with a relative accuracy of 5×10^{-2} (Extended Data Fig. 4c, d); and nonlinear compression using imperfection, where to study metamaterials in which β links have an offset δ_β we compress the structure up to a strain of 6.6% (Extended Data Fig. 5).

Experimental techniques. We used 10-mm-thick cast sheets of silicone rubber (shore 80A, Silex Silicones LTD, Young's modulus $E = 8$ MPa), which are sufficiently stiff to ensure minimal affects from gravity and exhibit minimal viscous and creeping effects. We fabricated the samples using a water-jet cutter, gluing the rubber to 10-mm-thick plywood boards to ensure precise cutting. We then marked each internal square (side length of 4.5 mm) of the sample with an ellipse (2.5 mm × 4 mm) for detection purposes.

The hinges between each square consist of rectangular cuboid beams of height 10 mm (same at the sheet thickness) and lateral thickness t_α, t_β or t_γ. Irrespective of the beams, the (virtual) corners of the squares meet precisely in a point—the beams add material to this idealized design (Extended Data Fig. 7). The thicknesses t_α, t_β and t_γ range from 0.8 mm to 4.0 mm depending on the nature of the link (α, β or γ) and on the sample (see main text and Methods section 'Design guidelines and experimental validation' for specifications). In some runs, we offset the beams laterally by $\delta_\beta = t_\beta/2$, leading to triangular-shaped links. The rank-2 (rank-3) metamaterials shown in Figs. 1, 2 (Fig. 3) consist of 4×4 (3×3) unit cells, namely 80 (225) internal squares.

The samples were tested under equi-biaxial compression. To this end, we used a custom-made aluminium V-shaped press (see Extended Data Fig. 8) that was carefully positioned and aligned in a universal testing machine (Instron 3366) equipped with a 1-kN load cell, which enabled us to impose a compressive displacement with 10-μm accuracy and to record the force with 0.1-N accuracy. We used fine powder to reduce the friction at the boundaries as much as possible.

The pictures were recorded using a high-resolution complementary metal–oxide–semiconductor (CMOS) camera (3,858 pixels × 2,764 pixels, Basler acA3800-14um), equipped with a 75-mm prime lens (KOWA; LM50HC 1″) for the rank-2 metamaterial and with a 50-mm prime lens (KOWA; LM75HC 1″) for the rank-3 metamaterial, paired with custom-made LED-based front- and back-light systems. To minimize reflections from the front light, the V-press glass windows are coated.

Image tessellation techniques. The images were processed using standard image tessellation and tracking techniques to extract the positions of the squares and the bending angles of the links that connect the squares. In particular, using a semi-automatic custom-made tracking algorithm, special attention was devoted to obtain space–time trajectories of nearly all squares and bending angles (see Supplementary Videos 1 and 2). Inevitable detection errors occurred close to the edges of the compression cell and when squares came in contact, which led to flickering of the positions and orientation of the squares and therefore of the bending angles. To address this issue, events with angle fluctuations of more than 10° between two consecutive frames were filtered out. We verified that the value of the filtering threshold has only a minor effect on the data.

In addition, as discussed in the main text, friction and frustration at the boundary inevitably cause distortions and misfoldings, the description of which is beyond the scope of this work. Therefore, to compute the bending angles shown in Fig. 2d, h, l, p (Fig. 3), we restrict our attention to a region of interest comprising the 28 (29) most central squares for the rank-2 (rank-3) metamaterial. In Extended Data Fig. 9 we show the same data, but calculated over a much wider area, comprising 64 (165) squares. Even though the scatter is larger, the main trends and multi-step nature are still apparent in these data.

Sequential pathways with alternative topologies. To demonstrate that sequential pathways are not limited to the hierarchical structures under biaxial compression shown in the main text, we constructed two alternative geometries that exhibit a two-step pathway under uniaxial compression, using the same rubber and water-jetting technique as for the samples shown in the main text (see Extended Data Fig. 10). The basic idea is to couple two groups of links with different buckling thresholds in series, so that under compression the two types of link buckle in sequence. In one geometry, we use a diluted square lattice consisting of two rows of coupled columns with different link thicknesses (Extended Data Fig. 10a). Under compression, we observe that the columns with the thinnest links buckle first, then fold up until self-contacts are created, and finally trigger the buckling of the other columns with thicker links. Because this structure is soft to lateral shear, we use lateral sliding boundaries. In the second geometry, we use a variation that removes the soft shear modes, so that no lateral boundaries are required; here, a clear two-step sequence is also observed (Extended Data Fig. 10b). These alternative designs demonstrate that the combination of buckling and self-contacts can generate sequential pathways in various structures.

Data and code availability. The data shown in the figures and the data and code that support the other findings of this study are available from the corresponding author on request.

31. Coulais, C. Periodic cellular materials with nonlinear elastic homogenized stress-strain response at small strains. *Int. J. Solids Struct.* **97–98**, 226–238 (2016).

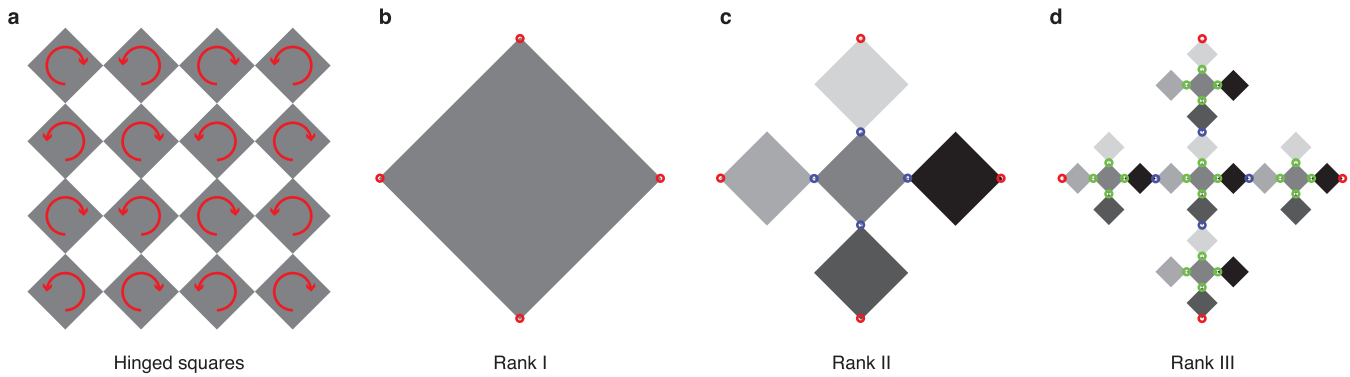

Extended Data Fig. 1 | Multimodal hierarchical mechanical metamaterials. a, 4×4 rotating-square mechanism, which has a zero mode corresponding to counter-rotation of each square unit as indicated. **b–d**, Hierarchical construction of a box fractal, where in each generation a square is replaced by a cross-like pattern of five smaller squares. Red, blue and green links correspond to α links that connect different units, internal β links that occur for rank $m \geq 2$ and γ links that occur for rank $m \geq 3$, respectively.

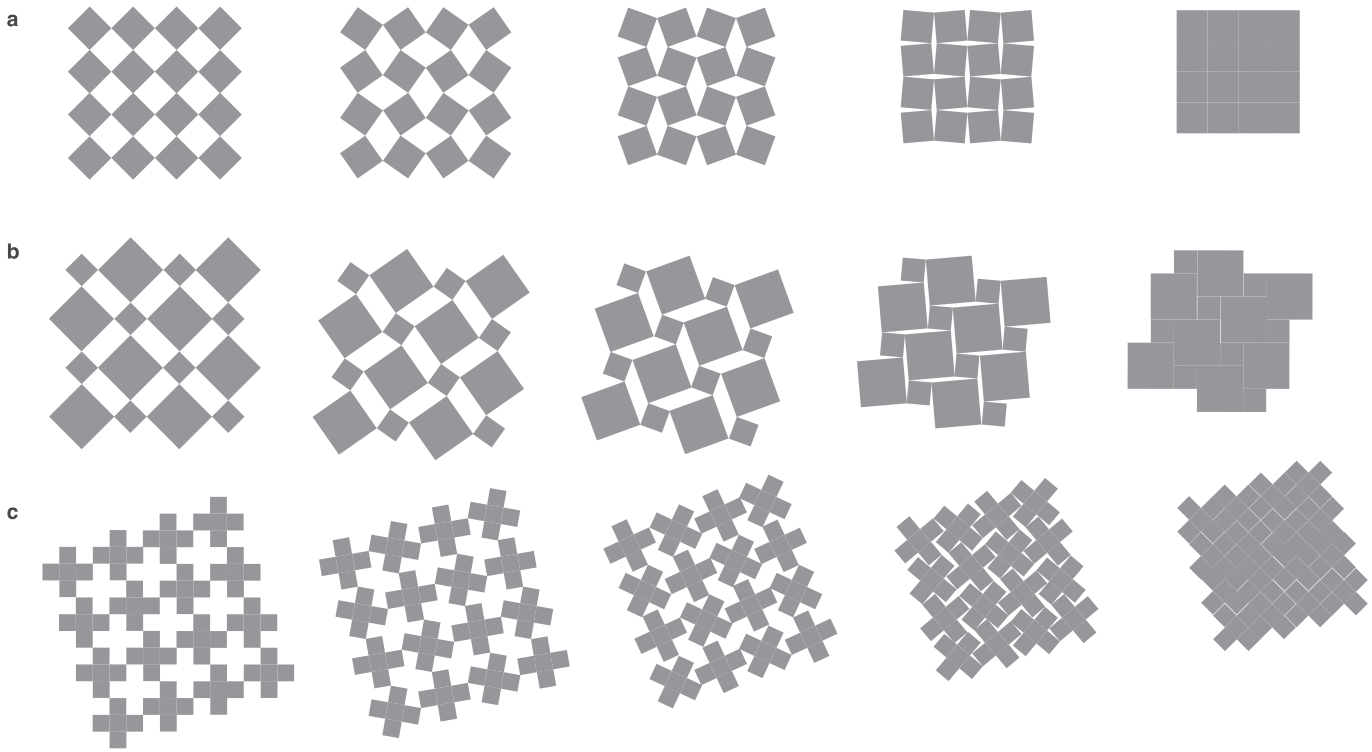

Extended Data Fig. 2 | Hinged tessellations. a, Free motion of the rotating-square mechanism. **b**, Free motion of rotating-square mechanism with unequal squares. **c**, Free motion of linked crosses.

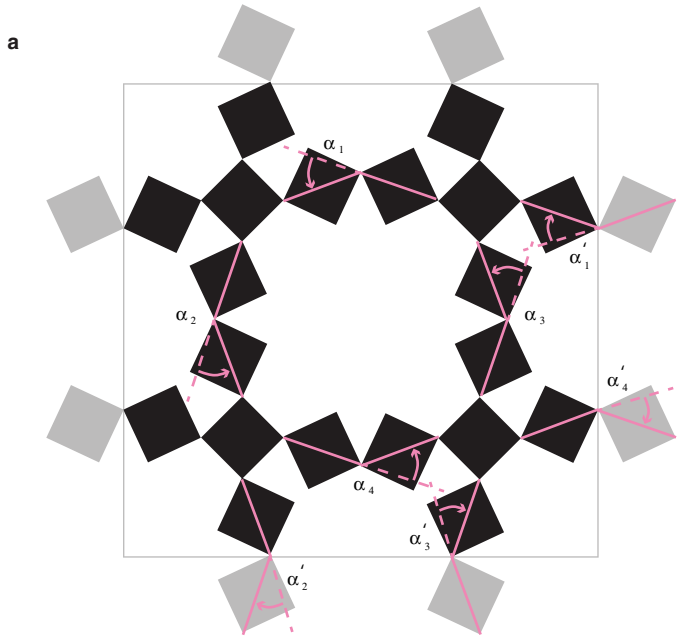

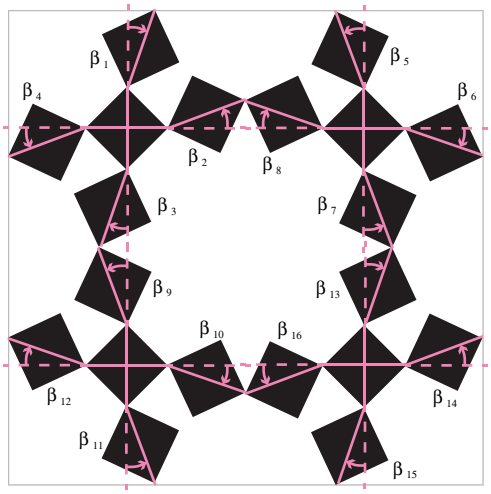

c

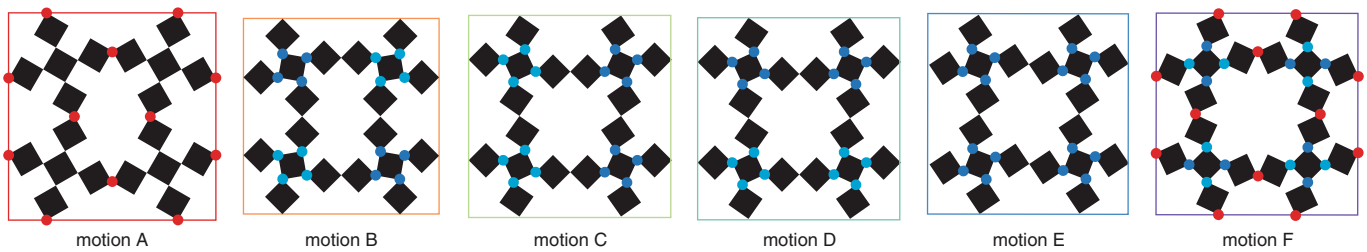

d

vectors	α_1	α_2	α_3	α_4	α'_1	α'_2	α'_3	α'_4	β_1	β_2	β_3	β_4	β_5	β_6	β_7	β_8	β_9	β_{10}	β_{11}	β_{12}	β_{13}	β_{14}	β_{15}	β_{16}
$\mathbf{m}_A$	1	−1	−1	1	−1	1	1	−1	0	0	0	0	0	0	0	0	0	0	0	0	0	0	0	0
$\mathbf{m}_B$	0	0	0	0	0	0	0	0	−1	−1	−1	−1	1	1	1	1	1	1	1	1	−1	−1	−1	−1
$\mathbf{m}_C$	0	0	0	0	0	0	0	0	1	1	1	1	−1	−1	−1	−1	1	1	1	1	−1	−1	−1	−1
$\mathbf{m}_D$	0	0	0	0	0	0	0	0	−1	−1	−1	−1	−1	−1	−1	−1	1	1	1	1	1	1	1	1
$\mathbf{m}_E$	0	0	0	0	0	0	0	0	−1	−1	−1	−1	−1	−1	−1	−1	−1	−1	−1	−1	−1	−1	−1	−1
$\mathbf{m}_F$	2	2	2	2	−2	−2	−2	−2	−1	1	−1	1	1	−1	1	−1	1	−1	1	−1	−1	1	−1	1

Extended Data Fig. 3 | Kinematics and orthogonal basis of zero-energy motions of a 2 × 2 super-cell with square periodic boundary conditions. **a**, Definition of the bending angles $\{\alpha_1, \alpha_2, \alpha_3, \alpha_4, \alpha'_1, \alpha'_2, \alpha'_3, \alpha'_4\}$. The grey squares depict the periodic boundary conditions. **b**, Definition of the angles $\{\beta_1, \beta_2, \ldots, \beta_{16}\}$. **c**, **d**, The motions A–F form an orthogonal basis of deformations. **c**, Schematic representation. Red denotes hinging of the α links. Light (dark) blue denotes clockwise (anticlockwise) hinging of the β links. **d**, Vector representation. The row of the table correspond to the vectors $\boldsymbol{m}_{A,\ldots,F} = \{\alpha_1, \ldots, \alpha_4, \alpha'_1, \ldots, \alpha'_4, \beta_1, \ldots, \beta_{16}\}$ that form the basis of all possible motions A–F.

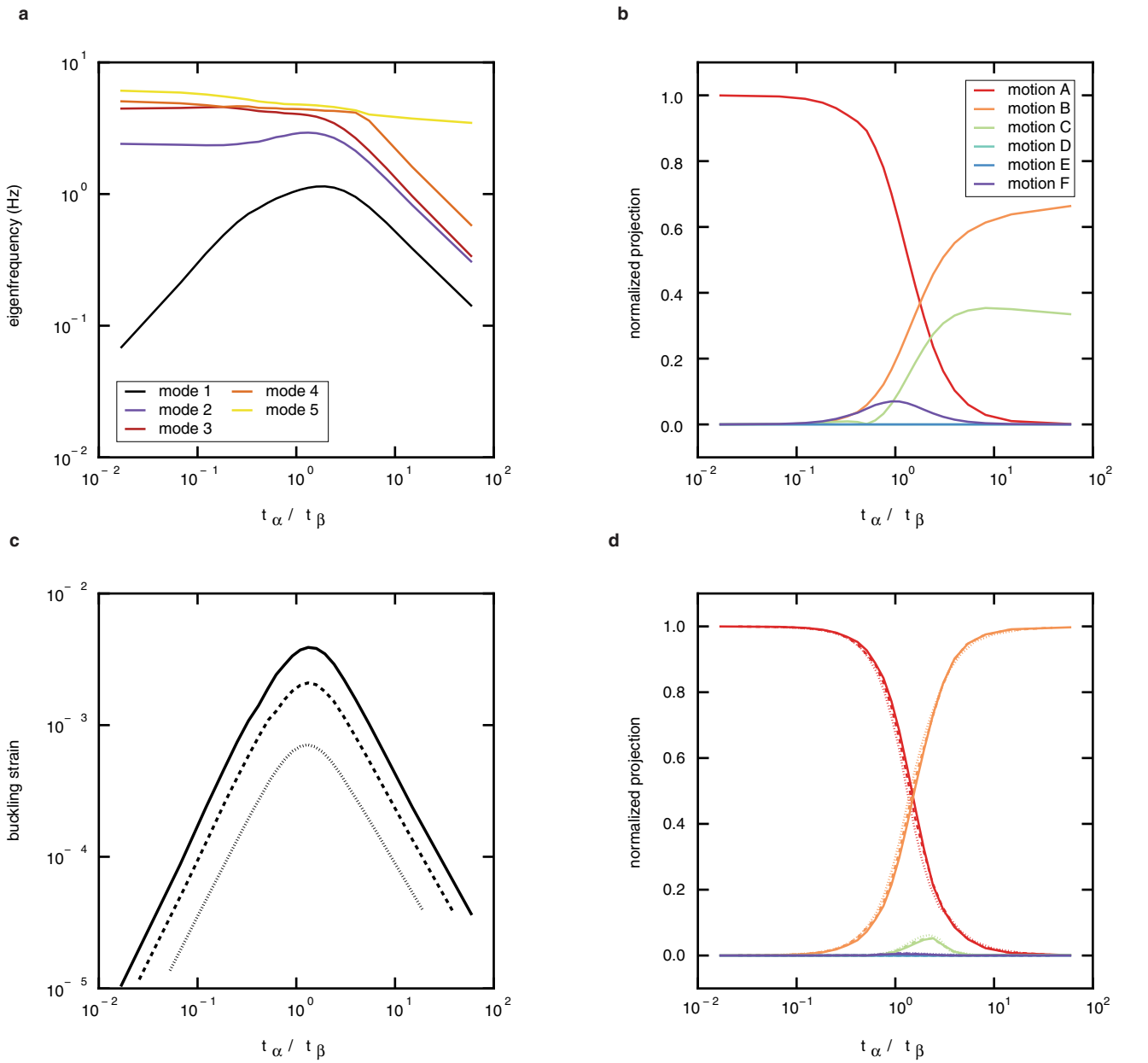

Extended Data Fig. 4 | Mode analysis for a 2 × 2 super-cell with square periodic boundary conditions. Unless noted otherwise, all data are for $t_\alpha + t_\beta = 3$ mm; data for other normalizations look extremely similar. **a**, Eigenfrequencies of the first linear eigenmodes as functions of t_α/t_β. **b**, Normalized projection of the lowest eigenmode onto motions A–F. To calculate the normalized projections, we compute the inner products between the bending-angle vectors $\boldsymbol{b}$ and the vectors $\boldsymbol{m}_{A,\ldots,F}$ defined in Extended Data Fig. 3 and normalize them by the sum of all inner products. **c**, Critical buckling strain as a function of t_α/t_β, for $t_\alpha + t_\beta = 1$ mm, 2 mm and 3 mm (dotted, dashed and solid lines, respectively). The value of the critical strain depends on $t_\alpha + t_\beta$, but the crossover does not. **d**, Normalized projection of the buckling mode onto motions A–F, for $t_\alpha + t_\beta = 1$ mm, 2 mm and 3 mm (dotted, dashed and solid lines, respectively). We calculate the normalized projections as in **c**.

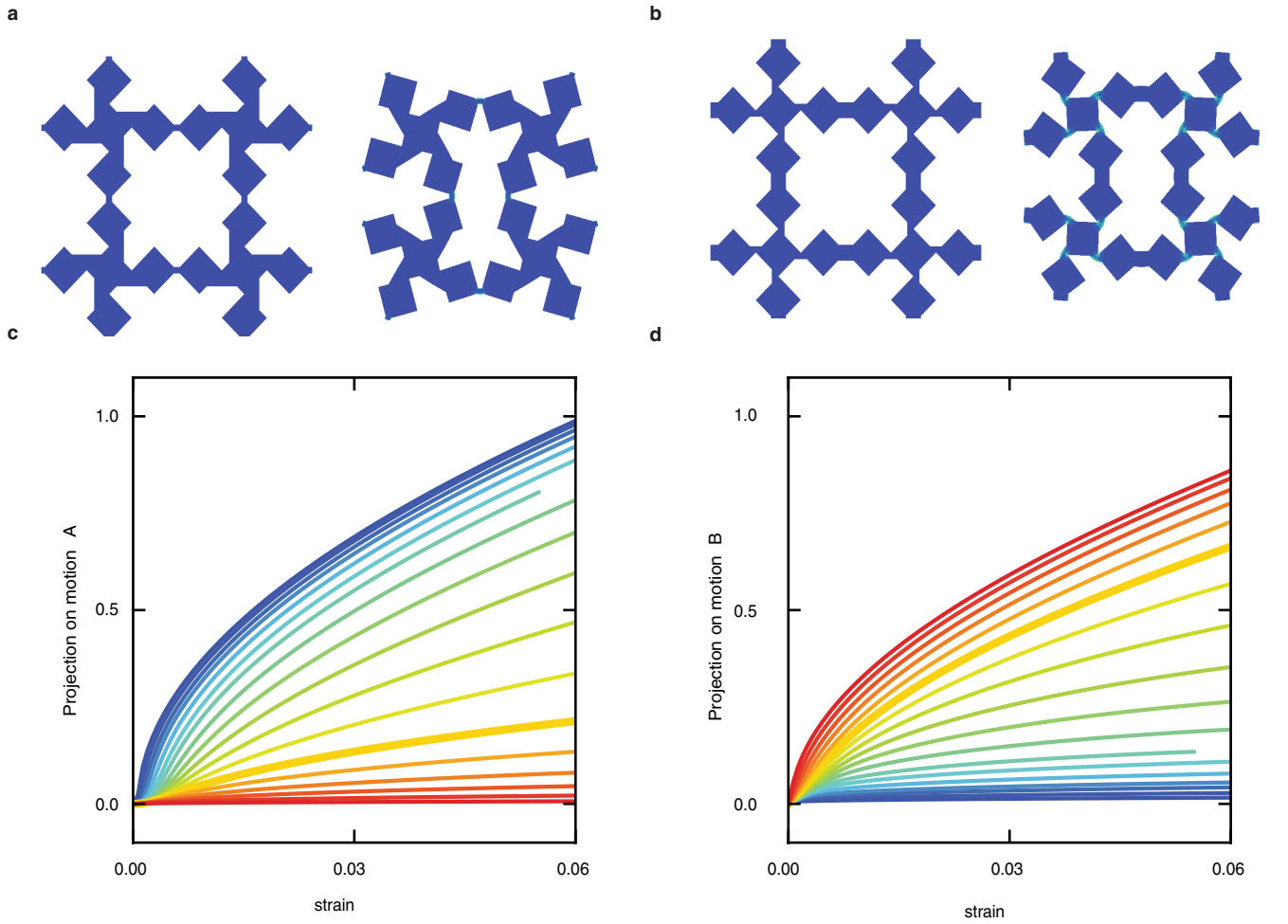

Extended Data Fig. 5 | Nonlinear analysis with symmetry-broken links on a 2 × 2 super-cell with square periodic boundary conditions. **a**, **b**, Snapshots of the super-cell in the un-deformed (left) and deformed (strain of 6.6%; right) states, for $t_\alpha = 0.9$ and $t_\beta = 2.1$ (**a**) and $t_\alpha = 2.1$ and $t_\beta = 0.9$ (**b**). In both cases, the offset of the β links is $0.5t_\beta$. **c**, **d**, Projection of the deformed states $\boldsymbol{b} \cdot \boldsymbol{m}_A$ (**c**) and $\boldsymbol{b} \cdot \boldsymbol{m}_B$ (**d**) versus strain ε for t_α/t_β ranging from 0.2 (blue) to 15 (red) and $t_\alpha + t_\beta = 3$ mm. The case $t_\alpha/t_\beta = 2.3$, which is close to the experimental value ($t_\alpha/t_\beta = 2.5$, Fig. 2e–h) is highlighted by a thick yellow line.

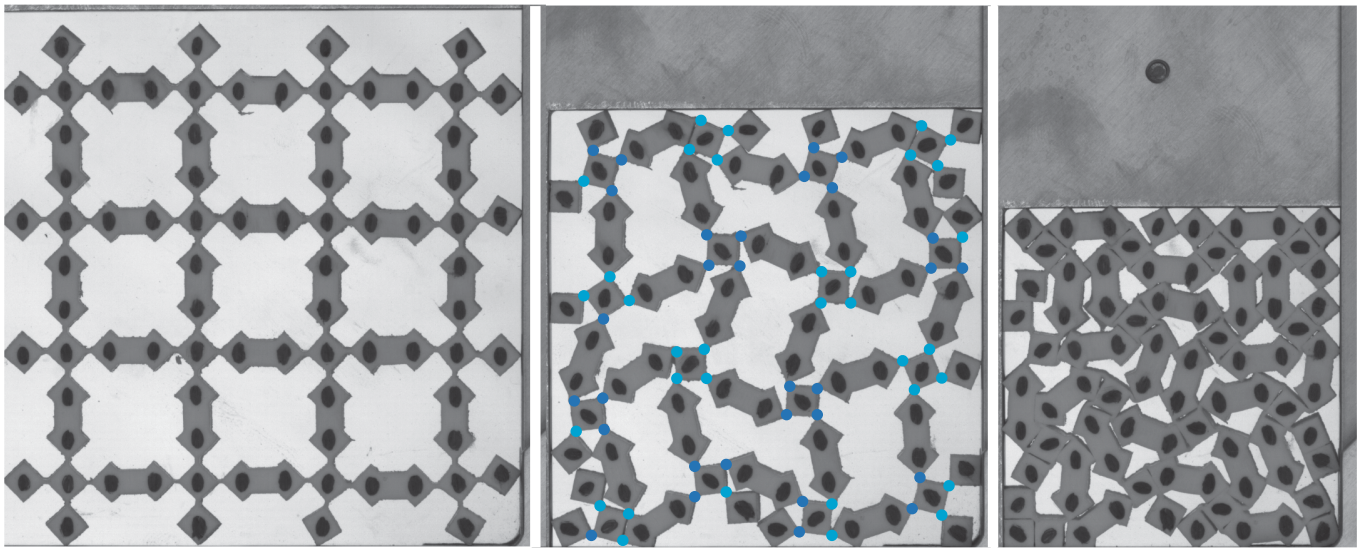

Extended Data Fig. 6 | Metamaterial under compression with $t_\alpha = 4$ mm and $t_\beta = 1$ mm. Stills of the compression experiment are shown for strains of $\varepsilon = 0$ (left), 0.24 (middle) and 0.52 (right). In the middle panel, the light (dark) blue dots indicate clockwise (anticlockwise) hinging of the β links, similar to motion B that initiates pathway II, but with substantial disorder near the boundaries that penetrate into the bulk.

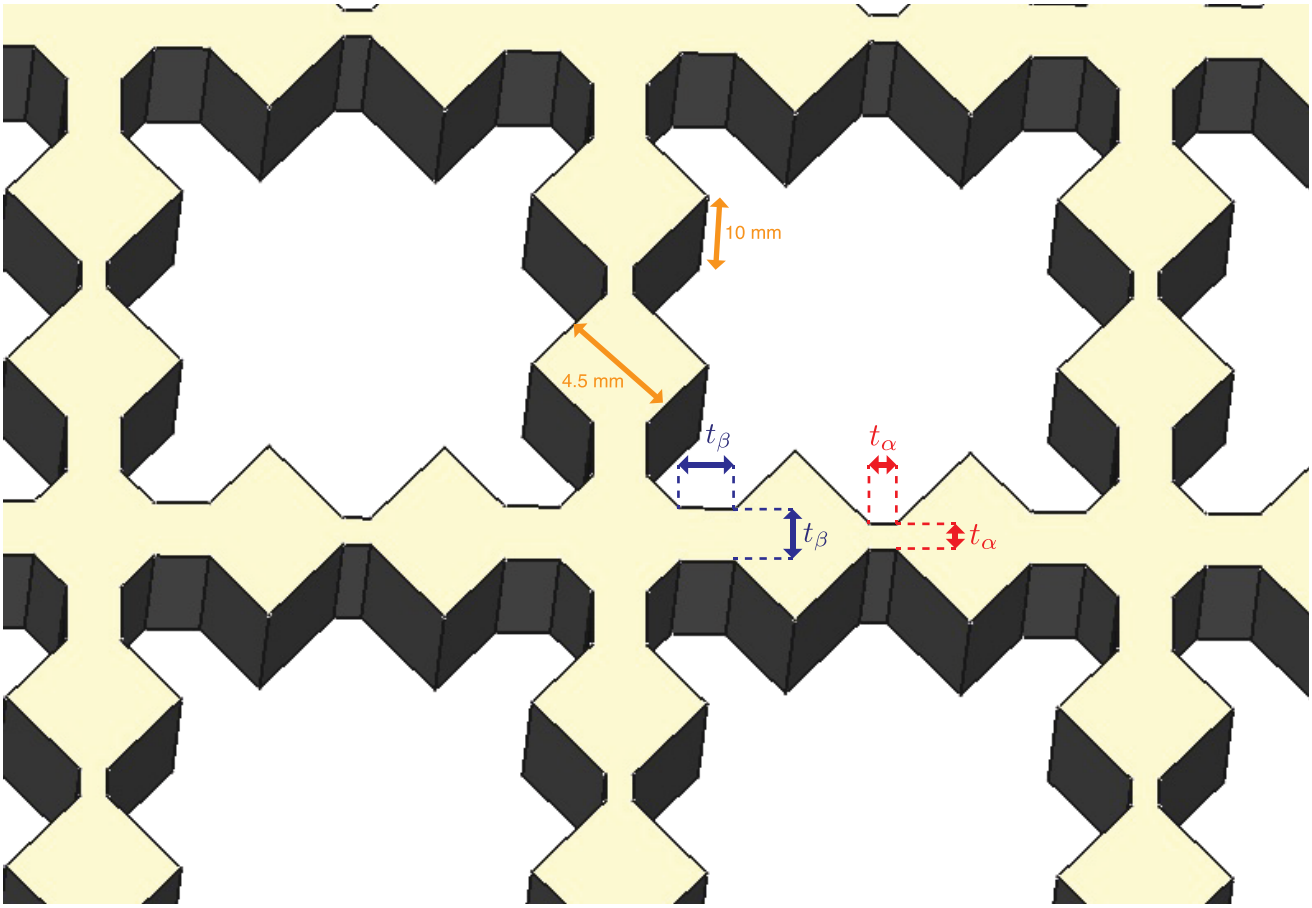

Extended Data Fig. 7 | Sample geometry. A close-up of the computer-assisted design of the rank-2 metamaterial is shown for the sample in Fig. 2a–d.

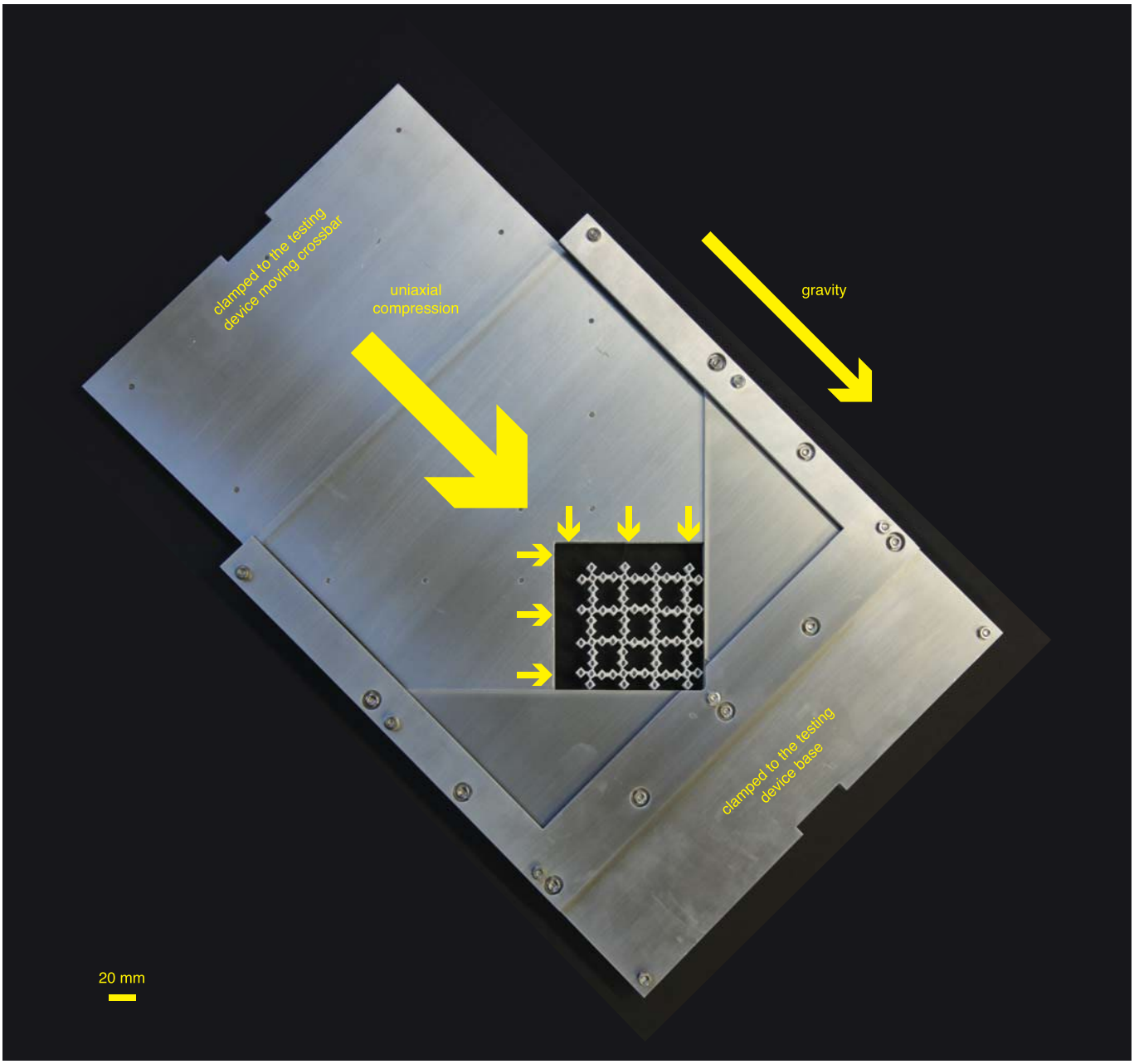

Extended Data Fig. 8 | Compression device. The custom-made compression fixture applies biaxial compression using a uniaxial testing device.

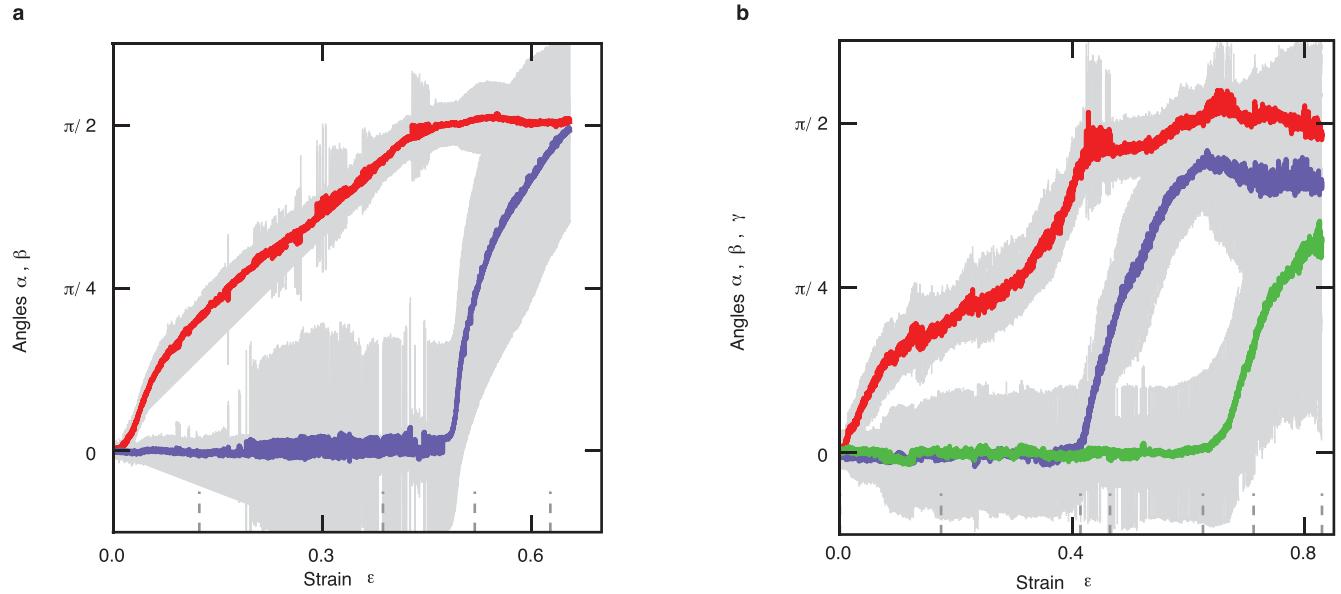

Extended Data Fig. 9 | Effect of boundaries on angles. a, **b**, Bending of the links for larger regions of the sample than shown in the main text: α (red) and β (blue) versus strain ε for the central 64 squares (excluding the outermost 16 squares) (**a**); α (red), β (blue) and γ (green) versus strain ε for the central 165 squares (excluding the outermost 60 squares) (**b**). Grey shading indicates one standard deviation and the angles are based on the same runs as in Fig. 2a–d (**a**) or Fig. 3 (**b**).

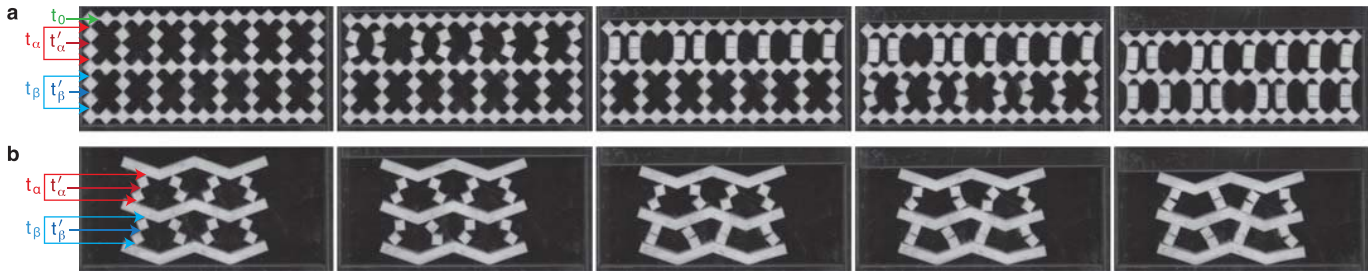

Extended Data Fig. 10 | Alternative topologies. a, Linked squares with edges of 4.5 mm and link thicknesses of $t_0 = 1.35$ mm, $t_\alpha = 0.45$ mm, $t'_\alpha = 0.45$ mm, $t_\beta = 0.9$ mm and $t'_\beta = 0.68$ mm, showing a two-step folding pathway under uniaxial compression. **b**, Structure of linked squares with edges of 4.5 mm and link thicknesses of $t_\alpha = 0.45$ mm, $t'_\alpha = 0.45$ mm, $t_\beta = 0.9$ mm and $t'_\beta = 0.9$ mm connected by slanted bars of thickness 4.5 mm, showing a two-step folding pathway under uniaxial compression.